Geophysical Journal International

Geophys. J. Int. (2019) **218,** 2054–2065
Advance Access publication 2019 June 10
GJI Geomagnetism, Rock Magnetism and Palaeomagnetism

doi: 10.1093/gji/ggz254

Mantle-induced temperature anomalies do not reach the inner core boundary

Christopher J. Davies and Jon E. Mound

School of Earth and Environment, University of Leeds, Leeds LS2 9JT, UK. E-mail: c.davies@leeds.ac.uk

Accepted 2019 June 7. Received 2019 March 1; in original form 2018 December 4

SUMMARY

Temperature anomalies in Earth's liquid core reflect the vigour of convection and the nature and extent of thermal core–mantle coupling. Numerical simulations suggest that longitudinal temperature anomalies forced by lateral heat flow variations at the core–mantle boundary (CMB) can greatly exceed the anomalies that arise in homogeneous convection (i.e. with no boundary forcing) and may even penetrate all the way to the inner core boundary. However, it is not clear whether these simulations access the relevant regime for convection in Earth's core, which is characterized by rapid rotation (low Ekman number E) and strong driving (high Rayleigh number Ra). We access this regime using numerical simulations of non-magnetic rotating convection with imposed heat flow variations at the outer boundary (OB) and investigate the amplitude and spatial pattern of thermal anomalies, focusing on the inner and outer boundaries. The 108 simulations cover the parameter range $10^{-4} \leq E \leq 10^{-6}$ and $Ra = 1-800$ times the critical value. At each Ra and E we consider two heat flow patterns—one derived from seismic tomography and the hemispheric Y_1^1 spherical harmonic pattern—with amplitudes measured by the parameter $q^\star = 2.3$, 5 as well as the case of homogeneous convection. At the OB the forcing produces strong longitudinal temperature variations that peak in the equatorial region. Scaling relations suggest that the longitudinal variations are weakly dependent on E and Ra and are much stronger than in homogeneous convection, reaching $O(1)$ K at core conditions if $q^\star \approx 35$. At the inner boundary, latitudinal and longitudinal temperature variations depend weakly on Ra and $q^\star$ and decrease strongly with E, becoming practically indistinguishable between homogeneous and heterogeneous cases at $E = 10^{-6}$. Interpreted at core conditions our results suggest that heat flow variations on the CMB are unlikely to explain the large-scale variations observed by seismology at the top of the inner core.

Key words: Core dynamics; Core-mantle boundary; Core-mantle coupling; Core flow; Earth's magnetic field.

1 INTRODUCTION

Convection in Earth's liquid core sustains Earth's magnetic field through a dynamo process that converts kinetic energy into magnetic energy. The convection is driven by thermal and chemical buoyancy forces and the associated thermochemical anomalies contain important information regarding the operation of the dynamo and the dynamics of the core. Radial variations reflect the vigour of core convection and the relative strength of thermal and chemical driving (Lister & Buffett 1995). Seismically slow regions observed at the top and bottom of the core (Souriau & Calvet 2015) have been argued to reflect departures from uniform composition (Gubbins *et al.* 2008; Helffrich & Kaneshima 2010; Gubbins & Davies 2013; Brodholt & Badro 2017; Wong *et al.* 2018), though thermal effects inevitably explain some of the signal. Lateral variations, particularly in longitude, may reflect coupling of core convection to temperature variations in the lowermost mantle (Buffett 2007). A key question is whether lateral variations in temperature imposed by mantle structure at the core–mantle boundary (CMB) persist to the inner core boundary (ICB) where a striking hemispheric variation in seismic properties is observed (Aubert *et al.* 2008; Monnereau *et al.* 2010; Gubbins *et al.* 2011; Souriau & Calvet 2015). The main obstacle in assessing this hypothesis is that the thermal structure of the core cannot be imaged directly and is difficult to disentangle from chemical variations. In this paper we use numerical simulations to investigate the magnitude and pattern of thermal anomalies in the core induced by heat flow variations at the CMB.

Radial temperature variations in the core are predominantly due to adiabatic compression (Jones 2015). The superadiabatic temperature difference ΔT_s between the CMB and ICB is usually assumed to

be accommodated by thermal boundary layers at the top and bottom of the core that are a matter of metres thick, with an adiabatic bulk interior (Jones 2015). Taking a superadiabatic temperature gradient across these layers comparable to the adiabatic gradient of 1 K km^{-1} (Davies *et al.* 2015) and assuming an adiabatic bulk gives $\Delta T_s \sim 10^{-2}$–10^{-3} K. Numerical simulations of spherical shell (Gastine *et al.* 2016; Mound & Davies 2017) and plane layer (Julien *et al.* 2012a,b) rotating convection display non-zero interior temperature gradients, which can account for as much as half of the total superadiabatic temperature drop in the plane layer case, though this does not significantly affect the estimate of ΔT_s. Variations in composition with depth are harder to estimate and are usually neglected altogether (Jones 2015).

With uniform thermal boundary conditions (referred to here as 'homogeneous' convection) lateral variations in temperature and composition within the core are expected to be tiny. Stevenson (1987) estimated that the density fluctuations associated with core convection are 9 orders of magnitude smaller than the mean density. Bloxham & Gubbins (1987) assumed a thermal wind balance just below the CMB and found that temperature anomalies of $O(10^{-3})$ K could account for core flows of $O(10)$ km yr^{-1} (see also Bloxham & Jackson 1990). These thermal anomalies are 6–7 orders of magnitude smaller than estimates of the adiabatic temperature at the CMB (Davies *et al.* 2015) and comparable to the estimate of ΔT_s. Based on estimates of the respective buoyancy fluxes, compositional buoyancy can exceed the thermal buoyancy that drives the core flow (Lister & Buffett 1995), though the magnitude of the chemical anomalies will be about 5 orders of magnitude smaller than their thermal counterparts owing to the much larger compositional expansivity (Gubbins *et al.* 2004).

Heterogeneous convection arising due to lateral variations in heat flow imposed on the core by the mantle may significantly alter the estimates above. Seismic tomographic images of the lowermost mantle clearly identify two regions beneath Africa and the central Pacific characterized by seismic velocity anomalies that are several per cent slower than predicted from 1-D models (e.g. Masters *et al.* 1996; Grand *et al.* 1997; Garnero & McNamara 2008; Hernlund & McNamara 2015). The precise nature of these anomalies is still debated, but there is general consensus that they at least partly reflect thermal variations in the lowermost mantle (Gubbins 2003; Garnero *et al.* 2016). Since thermal anomalies in the mantle greatly exceed those in the core the former produce lateral variations in the heat flow across the CMB with seismically slow regions corresponding to locally depressed heat flow and fast regions corresponding to locally elevated heat flow (e.g. Gubbins 2003; Olson 2003). The amplitude of the heat flow anomalies cannot be observed directly, but some numerical simulations suggest that the lateral variations exceed the average CMB heat flow (Nakagawa & Tackley 2007). However, unlike homogeneous convection, even infinitesimal boundary forcing will drive thermal wind flows that transport heat both laterally and into the interior (e.g. Zhang & Gubbins 1992; Shishkina *et al.* 2016).

In non-magnetic rotating convection the effect of imposed boundary forcing depends on the forcing pattern and amplitude, the Rayleigh number Ra measuring the vigour of homogeneous convection, the Ekman number E measuring the ratio of viscous to rotational effects, and the Prandtl number Pr measuring the ratio of viscous and thermal diffusion. In this paper we consider two large-scale heat flow patterns: (1) the pattern inferred by assuming that shear wave velocity variations in the lowermost mantle reflect thermal heterogeneity (the 'tomographic' pattern), which is dominated by spherical harmonic degree and order 2 (Masters *et al.* 1996); (2) the hemispheric spherical harmonic Y_1^1 pattern, which has been advocated as the large-scale pattern during supercontinent formation (Zhong *et al.* 2007). At low Ra, moderate $E \sim 10^{-3} - 10^{-5}$ and $Pr \gg 1$ these forcings produce quasi-periodic solutions with convection rolls clustered under high boundary heat flow regions instead of the usual pattern of drifting uniformly spaced rolls (Davies *et al.* 2009). Time-dependent solutions emerge with decreasing E (Davies *et al.* 2009), decreasing Pr (Zhang & Gubbins 1996), increasing Ra (Sun *et al.* 1994) or the addition of a magnetic field (Gubbins *et al.* 2007; Sreenivasan 2009). As Ra increases the boundary effects become harder to identify in snapshots, though they can be clearly seen in time-averages (Sun *et al.* 1994; Olson & Christensen 2002; Aubert *et al.* 2007) and we will hence use averages throughout this paper. The main effect of large-scale boundary forcing in the parameter regime studied to date is to induce longitudinal variations in the time-averaged core surface flow and magnetic field (e.g. Bloxham 2000; Christensen & Olson 2003; Olson 2003; Davies *et al.* 2008; Mound *et al.* 2015; Olson *et al.* 2017). Longitudinal thermal structure, the focus of this paper, has received less attention though a recent study predicts temperature variations of $O(1)$ K at the CMB in geodynamo simulations with strong boundary forcing and imposed stable stratification (Christensen 2018), much larger than estimates based on homogeneous convection.

The influence of lateral CMB heat flow variations may not be confined to the uppermost regions of the core. Aubert *et al.* (2008), Gubbins *et al.* (2011) and Sreenivasan & Gubbins (2011) found that columnar boundary-induced flows would leave an imprint on the inner core, producing localized melting and freezing at the ICB. This mechanism has been invoked as a possible explanation for the laterally heterogeneous structure observed at the top of the inner core (Niu & Wen 2001; Waszek *et al.* 2011; Souriau & Calvet 2015). In this paper, we will quantify the strength and structure of thermal variations at the ICB across a broad range of model parameters.

Numerical simulations of core convection and dynamo action cannot model the small diffusivities that describe molecular transport processes in Earth's core. Systematic studies, rather than individual model runs, are needed to establish the effect of changing control parameters on the time-averaged properties. This is particularly challenging when considering heterogeneous boundary conditions as extra parameters (the pattern and amplitude of the lateral variations) must be varied compared to homogeneous models. The problem is further exacerbated since recent work on non-magnetic rotating convection shows that models with $E \geq 10^{-4}$, which represents the majority undertaken to date, do not access the rapidly rotating regime thought relevant to Earth's core (Gastine *et al.* 2016; Mound & Davies 2017). It is not currently practical to comprehensively study this regime with geodynamo simulations owing to the enormous computational costs (e.g. Matsui *et al.* 2016), but it can be accessed with non-magnetic models. A systematic study of non-magnetic boundary-forced convection has been achieved at $E = 5 \times 10^{-5}$ (Dietrich *et al.* 2016), but using a hemispheric heat flow pattern that is not directly related to present-day Earth.

We have recently produced a suite of 108 non-magnetic rotating convection simulations spanning the parameter range $10^{-4} \leq E \leq 10^{-6}$, $Ra_c \leq Ra < 800Ra_c$ and $Pr = 1$. Here Ra_c is the critical value of Ra for the onset of non-magnetic convection. At each E and Ra we have conducted simulations with hemispheric, tomographic and homogeneous outer boundary (OB) heat flow patterns. Of the 108 simulations, 106 are listed in Appendix B of Mound & Davies (2017) while new models with $E = 10^{-6}$, $Ra = 18\,000$, and a Y_1^1

heat flow pattern with two different forcing amplitudes have been conducted for this study. Heat transfer data suggest that the models with $E = 10^{-4}$ transition with increasing Ra from the weakly nonlinear regime involving a balance between viscous, Coriolis and buoyancy forces (Gillet & Jones 2006), directly to a regime where rotation plays a subdominant role (Gastine *et al.* 2016; Mound & Davies 2017). However, crucially, models at $E = 10^{-5}$ and 10^{-6} reach the rapidly rotating and strongly driven regime thought to describe core dynamics.

In this paper, we use the suite of models in Mound & Davies (2017) to quantify the magnitude and spatial structure of the time-averaged temperature, focusing on conditions at the top and bottom of the domain. We quantify latitudinal and longitudinal thermal variations and develop empirical scaling relations to gain insight into the thermal conditions that may pertain at the top and bottom of Earth's core. Model setup and outputs are described in Section 2 and results are presented in Section 3. A discussion of the limitations of our model and considerations required to apply the results to Earth are given in Section 4. Conclusions are presented in Section 5.

2 METHODS

2.1 Numerical model and parameters

Complete details of the numerical simulations used in this study can be found in Mound & Davies (2017) and so only a brief description is given here. The numerical code (Willis *et al.* 2007) employs spherical polar coordinates (r, θ, ϕ) and solves the equations governing conservation of mass, momentum and energy in a spherical shell that rotates about the vertical $\hat{\boldsymbol{z}}$ direction with constant angular frequency Ω. The dimensionless forms of these equations can be written, respectively, as

$$\boldsymbol{\nabla \cdot u} = 0, \tag{1}$$

$$\frac{E}{Pr}\left(\frac{\partial \boldsymbol{u}}{\partial t} + (\boldsymbol{u \cdot \nabla})\boldsymbol{u}\right) + \hat{\boldsymbol{z}} \times \boldsymbol{u} = -\nabla \tilde{P} + Ra T' \boldsymbol{r} + E\nabla^2 \boldsymbol{u}, \tag{2}$$

$$\frac{\partial T}{\partial t} + (\boldsymbol{u \cdot \nabla})T = \nabla^2 T, \tag{3}$$

where $\boldsymbol{u}$ is the fluid velocity, $\tilde{P}$ is the modified pressure, and $T = T_C + T'$ is the total temperature, where T_C is the temperature in the absence of motion and T' is the temperature perturbation. In writing the dimensionless equations we have assumed a constant kinematic viscosity ν, thermal diffusivity κ and thermal expansivity α, and scaled length by the shell thickness h, time by the thermal diffusion time $\tau_\mathrm{d} = h^2/\kappa$, and temperature by β/h. T_C satisfies the equation $\partial T_C/\partial r = -\beta/r^2$ and hence the parameter β is related to q_ave, the mean heat flow per unit area at r_o, by $q_\mathrm{ave} = -k\partial T_C/\partial r|_{r_\mathrm{o}} = k\beta/r_\mathrm{o}^2$ where k is the thermal conductivity.

The dimensionless parameters in eqs (1)–(3) are the Prandtl number Pr, the Ekman number E and the Rayleigh number Ra, which are defined as

$$Pr = \frac{\nu}{\kappa}, \quad E = \frac{\nu}{2\Omega h^2}, \quad Ra = \frac{\alpha g \beta}{2\Omega\kappa}. \tag{4}$$

In this study all models have $Pr = 1$, a ratio of inner boundary (IB) and OB radii $r_\mathrm{i}/r_\mathrm{o} = 0.35$ and a gravity profile that varies linearly with r such that $\boldsymbol{g} = -(g/r_\mathrm{o})\boldsymbol{r}$. The critical Rayleigh number depends on E: $Ra_c = 16.4$ at $E = 10^{-4}$, 24.7 at $E = 10^{-5}$ and 41.0 at $E = 10^{-6}$ (Mound & Davies 2017).

In all simulations the velocity boundary conditions are no-slip and fixed heat flux at r_i and r_o. There are three groups of simulations, defined by the pattern of heat flow heterogeneity imposed on the OB. The first, denoted by the letter '*H*', have homogeneous heat flow at r_o. The second, denoted by '*Y*', have an imposed pattern corresponding to the spherical harmonic degree and order 1, Y_1^1. The final group, denoted '*T*', have an imposed heat flow pattern derived from the seismic tomography model of Masters *et al.* (1996) assuming that the lateral shear-wave velocity variations reflect thermal heterogeneity in the lowermost mantle. The tomographic pattern is dominated by the spherical harmonic Y_2^2 component, but also contains other significant contributions such as Y_2^0. The amplitude of the lateral variations is defined by the parameter $q^\star$:

$$q^\star = \frac{q_\mathrm{max} - q_\mathrm{min}}{q_\mathrm{ave}}, \tag{5}$$

where q_max, q_min and q_ave are, respectively, the maximum, minimum and average heat flow through the OB. Mound & Davies (2017) considered values of $q^\star = 2.3$ and 5.0 (homogeneous cases correspond to $q^\star = 0$). We use the shorthand notation $Xq^\star = C$ to distinguish different model groups, where $X \in \{H, Y, T\}$ and $C = 0, 2.3, 5.0$.

Our numerical code utilizes a toroidal–poloidal decomposition to represent the vector velocity field. Scalar fields are expanded in spherical harmonics on spherical surfaces and finite-differences in radius. Fields are evolved in time using a predictor–corrector scheme with adaptive timestepping. The code successfully reproduces the dynamo benchmark solutions (Willis *et al.* 2007; Davies *et al.* 2011; Matsui *et al.* 2016). All solutions used in this study have been checked for spatial convergence, and run until robust time-averaged diagnostics of heat transfer behaviour were obtained (Mound & Davies 2017).

2.2 Diagnostics of temperature variations

We use several diagnostics to quantify latitudinal and longitudinal temperature variations at the IB and OB. Strong latitudinal variations can occur without heterogeneous boundary forcing, reflecting the efficiency of heat transport as well as the comparative vigour of convection inside and outside the tangent cylinder (Jones 2000). Longitudinal variations are expected to be weak in (time-averaged) homogeneous convection, but may be promoted by an imposed pattern of heat flow. Any influence of heterogeneous boundary conditions is expected to be most evident in time-averages, which we define by an overbar:

$$\bar{T}(r, \theta, \phi) = \frac{1}{t_1 - t_0}\int_{t_0}^{t_1} T(r, \theta, \phi, t)\mathrm{d}t, \tag{6}$$

where t_0 and t_1 are the start and end times, which usually span over 100 advection times (see Mound & Davies 2017, for details). Horizontal averages $\bar{T}_\mathrm{h}$ are defined as

$$\bar{T}_\mathrm{h}(r) = \frac{1}{4\pi}\int_S \bar{T}(r, \theta, \phi)\sin\theta \mathrm{d}\theta\mathrm{d}\phi. \tag{7}$$

We characterize latitudinal variations in $\bar{T}$ at each r and θ by

$$\bar{T}_\theta(r, \theta) = \frac{1}{2\pi}\int \bar{T}\mathrm{d}\phi - \bar{T}_\mathrm{h}. \tag{8}$$

The peak-to-peak amplitude at any radius is

$$\delta\bar{T}_\theta(r) = \max\left(\bar{T}_\theta(r, \theta)\right) - \min\left(\bar{T}_\theta(r, \theta)\right). \tag{9}$$

This is often, but not always, the pole-to-equator difference.

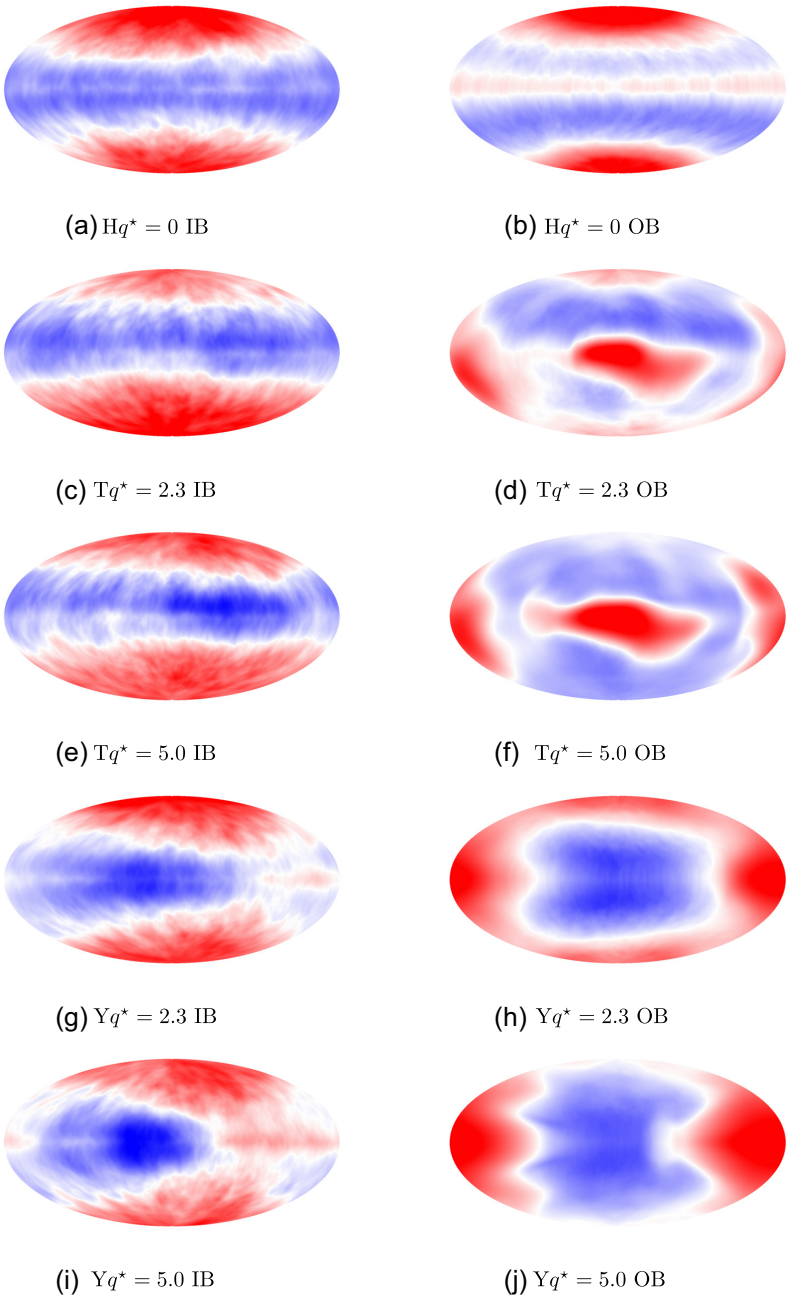

Figure 1. Temperature perturbation $\bar{T} - \bar{T}_{\rm h}$ at the inner boundary (left-hand panel) and outer boundary (right-hand panel). From top to bottom the rows show homogeneous boundaries (H), Tomographic boundaries (T) with $q^\star = 2.3$ and $q^\star = 5.0$, and Y_1^1 boundaries with $q^\star = 2.3$ and $q^\star = 5.0$. All runs have $E = 10^{-5}$ and $Ra = 13000 = 526 Ra_c$. Red (blue) is hotter (colder) than average.

We characterize longitudinal variations in $\bar{T}$ at each r and θ by

$$\bar{T}_\phi(r,\theta) = \max\left(\bar{T}(r,\theta,\phi)\right) - \min\left(\bar{T}(r,\theta,\phi)\right). \tag{10}$$

The largest longitudinal variation at any radius is

$$\delta\bar{T}_\phi(r) = \max\left(\bar{T}_\phi(r,\theta)\right). \tag{11}$$

When calculating differences between homogeneous and heterogeneous models the superscripts 'hom' and 'het' will be used, respectively; these will generally be omitted when there is no possibility of confusion.

Estimating the dimensional strength of temperature anomalies requires a temperature scale that can be observationally constrained. Here we use ΔT, the difference between $\bar{T}_{\rm h}$ on the OB and IB. We define

$$T^\star = \frac{\max\left(\bar{T}(r_{\rm o},\theta,\phi)\right) - \min\left(\bar{T}(r_{\rm o},\theta,\phi)\right)}{\Delta T} \tag{12}$$

as a dimensionless measure of the boundary temperature anomalies at the OB. An analogous expression is used at the IB.

In spherical shell convection with fixed flux boundaries ΔT is an output and varies significantly between models. In this configuration ΔT is related to the Nusselt number Nu by

$$Nu = \frac{\Delta T_c}{\Delta T}, \tag{13}$$

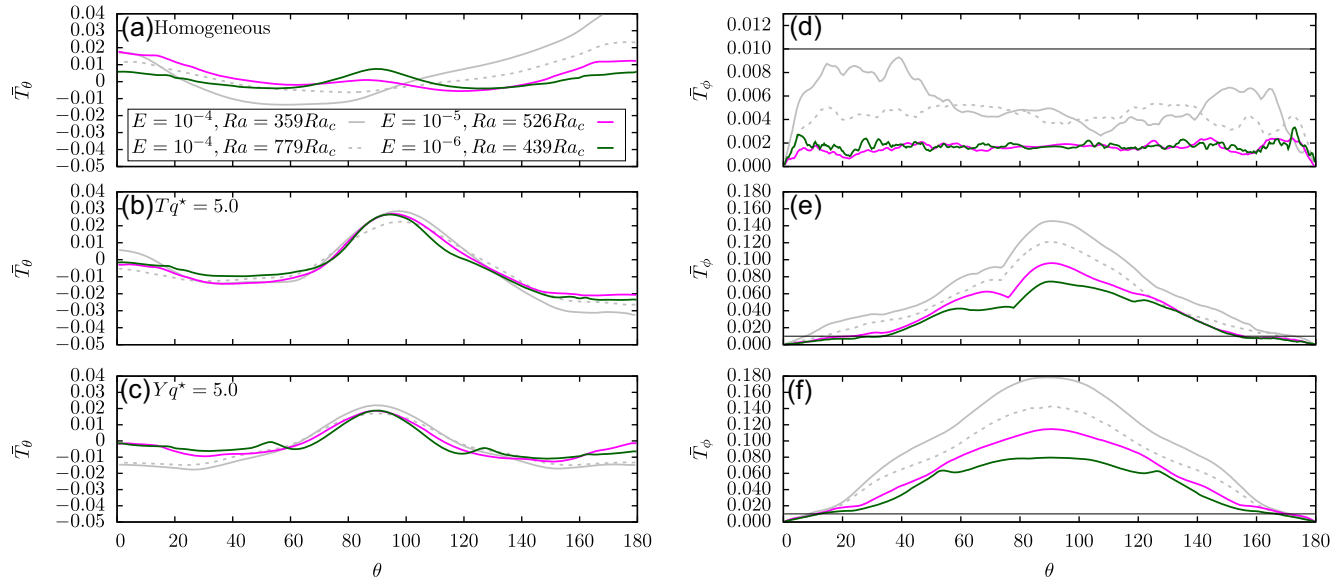

Figure 2. Longitudinal mean $\bar{T}_\theta$ (left-hand panel), and variation $\bar{T}_\phi$ (right-hand panel), of $\bar{T}$ as a function of latitude at the outer boundary. In each panel the top row shows homogeneous models, the middle row shows $Tq^\star = 5$ models and the bottom row shows $Yq^\star = 5$ models. Models are chosen to be of similar supercriticality Ra/Ra_c with two $E = 10^{-4}$ models shown that bracket the Ra/Ra_c values for $E = 10^{-5}$ and $E = 10^{-6}$. Left-hand plots have the same ordinate scale, while right-hand plots do not and so the 0.01 value of $\bar{T}_\phi$ is shown to aid comparison.

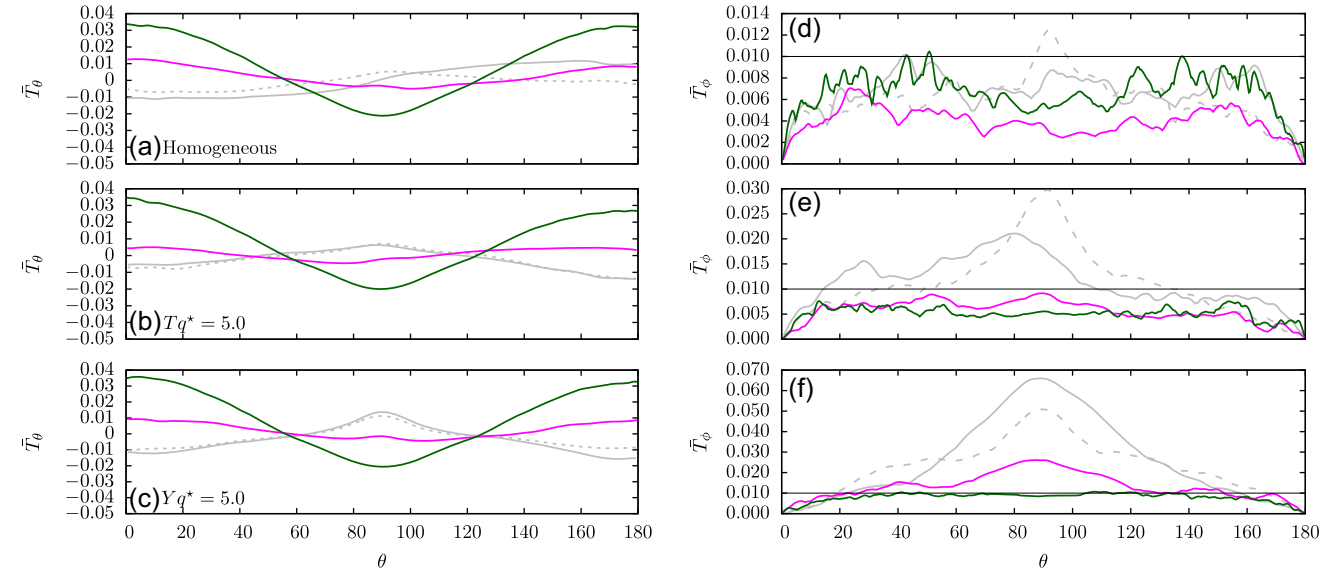

Figure 3. Same as Fig. 2 but at the inner boundary. Left-hand plots have the same ordinate scale, while right-hand plots do not and so the 0.01 value of $\bar{T}_\phi$ is shown to aid comparison.

(Mound & Davies 2017) where ΔT_c is the temperature difference between r_i and r_o due to conduction alone, that is when the velocity is zero. Therefore, an increase in the efficiency of convective heat transport corresponds to a decrease in ΔT.

3 RESULTS

In this section, we consider properties of the time-averaged temperature $\bar{T}$ at the IB and OB. We compare the latitudinal and longitudinal variations in $\bar{T}$ between models with homogeneous (H), tomographic (T) and Y_1^1 (Y) boundary patterns. We begin by presenting example cases with high Ra and low E before considering systematic behaviour as a function of Ra and E.

Fig. 1 shows examples of the time-averaged temperature perturbation $\bar{T} - \bar{T}_\mathrm{h}$ at the IB and OB for H, T and Y boundary patterns at $E = 10^{-5}$ and $Ra = 526Ra_c$. Considering first the OB, the poles are anomalously hot compared to the mid-latitudes in all models since convection is suppressed inside the tangent cylinder (the imaginary cylinder aligned with the rotation axis and tangent to the inner core equator, Jones 2000), though the effect weakens as $q^\star$ increases. In the homogeneous model $\bar{T}$ is dominantly axisymmetric and the equatorial region is anomalously cool, while in the heterogeneous models $\bar{T}$ clearly reflects the pattern of the boundary heat flow, with stronger anomalies at higher values of $q^\star$ as expected. At the IB $\bar{T}$ in the homogeneous model is similar to that at the OB, while in the tomographic models $\bar{T}$ is dominantly axisymmetric with little

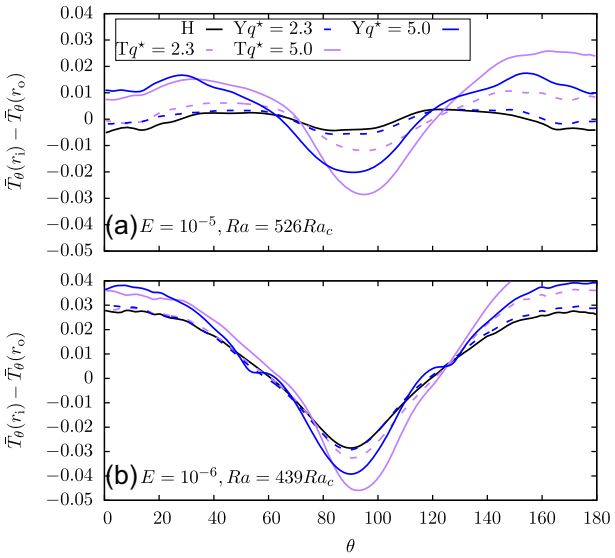

Figure 4. Difference between $\bar{T}_\theta$ at the IB and OB for two cases at low E and high Ra. Colours distinguish different patterns; dashed and solid lines show models with $q^\star = 2.3$ and $q^\star = 5.0$, respectively.

evidence of the Y_2^2 component seen at the OB. In these models the southern hemisphere is slightly hotter than the northern hemisphere (see also Figs 2 and 3), which reflects the slight displacement of the low heat flow regions on the OB towards the southern hemisphere. In the Y_1^1 models the pattern of OB heat flow can be distinguished in the equatorial region of the IB at these parameter values. Overall, the effect of the heterogeneous boundary conditions is more apparent at the OB than the IB.

To quantify latitudinal and longitudinal temperature variations at high Ra we plot $\bar{T}_\theta$ and $\bar{T}_\phi$ for models with different E and similar Ra/Ra_c. Figs 2 and 3 show results at the OB and IB, respectively, for H, T$q^\star$ = 5 and Y$q^\star$ = 5 models. Solutions with $E = 10^{-4}$ display several features not seen at lower E. First, homogeneous $E = 10^{-4}$ solutions display strong equatorial asymmetry, particularly at the OB, whereas at lower E, $\bar{T}_\theta$ is strongly equatorially symmetric (Fig. 2a). Secondly, homogeneous $E = 10^{-4}$ models display much stronger longitudinal variations in $\bar{T}_\phi$ at all latitudes on the OB than the lower E models (Fig. 2d). Thirdly, heterogeneous $E = 10^{-4}$ solutions display at equatorial maximum in $\bar{T}_\theta$ at the IB rather than a minimum seen at lower E (Figs 3a–c). These differences may reflect the fact that our $E = 10^{-4}$ models mainly access the weakly nonlinear and the non-rotating convective regimes, while the $E = 10^{-5}$ and 10^{-6} models mainly access the rapidly rotating regime (*cf.* Gastine *et al.* 2016; Mound & Davies 2017).

At the OB, higher values of $q^\star$ yield greater departures from the homogeneous case, with tomographic cases exhibiting the highest degree of equatorial asymmetry (Fig. 2), reflecting the imposed heat flow pattern. Thermal anomalies are enhanced in the equatorial region relative to the homogeneous case as expected. Latitudinal variations in $\bar{T}_\theta$ show little dependence on E, while the longitudinal variations are strongly dependent on E. The main effect of the heterogeneous boundary condition is to produce a hotter equator and colder poles at the OB compared to the homogeneous case. In the tomographic cases this arises because of the anomalously low heat flow regions under Africa and the Pacific, which suppress convection, and higher than average heat flux at higher latitudes. In the Y_1^1 cases this occurs because downwellings induced under the high heat flow hemisphere are narrower than upwellings induced under the low heat flow hemisphere (Mound & Davies 2017).

At the IB, several contrasting features to the OB results can be noted. First, departures from the homogeneous case are greatly reduced in all models and particularly in the $E = 10^{-6}$ cases where the heterogeneous and homogeneous models are barely distinguishable (Fig. 3). Second, the heterogeneous solutions are dominantly equatorially symmetric, even at $E = 10^{-4}$, for all forcing patterns. Third, latitudinal and longitudinal temperature variations depend strongly on E. In the higher E cases the heterogeneous boundary condition elevates $\bar{T}_\phi$ in the equatorial region, but even this signature is strongly reduced at $E = 10^{-6}$. In our low E and high Ra runs there are no morphological characteristics of the IB temperature that allow the homogeneous and heterogeneous cases to be meaningfully distinguished.

Temperature differences between the IB and OB reflect the efficiency of convective heat transfer and the thermal homogenization of the system. Fig. 4 shows $\bar{T}_\theta(r_\mathrm{i}) - \bar{T}_\theta(r_\mathrm{o})$ as a function of latitude for the low E models in Figs 2 and 3. The mean temperature at each radius has been subtracted and so $\bar{T}_\theta(r_\mathrm{i}) - \bar{T}_\theta(r_\mathrm{o}) < 0$ shows enhanced heat transport (reduced temperature difference). In the homogeneous models $\bar{T}_\theta(r_\mathrm{i}) - \bar{T}_\theta(r_\mathrm{o})$ in the polar regions decreases with increasing Ra/Ra_c, which probably reflects the steep increase in heat transfer with Ra associated with convection inside the tangent cylinder (Yadav *et al.* 2015). Compared to the homogeneous case, heterogeneous models have lower $\bar{T}_\theta(r_\mathrm{i}) - \bar{T}_\theta(r_\mathrm{o})$ in the equatorial region, reflecting enhanced heat transfer, and higher $\bar{T}_\theta(r_\mathrm{i}) - \bar{T}_\theta(r_\mathrm{o})$ in the mid- and high-latitude regions, reflecting reduced heat transfer. Increased heat transfer at low latitudes in heterogeneous simulations arises because the boundary heat flow variations promote strong correlations between the radial velocity and temperature (and hence the advective heat transport) which reduces the temperature gradient and hence ΔT (Mound & Davies 2017). At high-latitudes the imposed heat flow patterns contain much weaker anomalies and their effect is correspondingly reduced.

The maximum variation of $\bar{T}$ with longitude, $\delta\bar{T}_\phi$, is compared to the maximum variation with latitude, $\delta\bar{T}_\theta$, at the IB and OB in Fig. 5. Considering first the OB, $\delta\bar{T}_\phi/\delta\bar{T}_\theta$ is larger by at least an order of magnitude in heterogeneous compared to homogeneous cases and exceeds 1 in all heterogeneous cases when $Ra/Ra_c \geq 100$ (Fig. 5a). In general $\delta\bar{T}_\phi/\delta\bar{T}_\theta$ decreases with decreasing E, increases with $q^\star$ and increases weakly with Ra at high Ra (Fig. 5a). The variability in $\delta\bar{T}_\phi/\delta\bar{T}_\theta$ between the different imposed patterns and forcing amplitudes does not seem to depend significantly on E (Fig. 5c).

Significant differences are seen in $\delta\bar{T}_\phi/\delta\bar{T}_\theta$ at the IB compared to the OB. First, $\delta\bar{T}_\phi/\delta\bar{T}_\theta$ differs by only a factor of 2–5 between homogeneous and heterogeneous cases and is smaller than 1 in the majority of cases (Fig. 5b). The $E = 10^{-4}$ models are again exceptional, producing larger longitudinal temperature variations across a broad range of Ra/Ra_c. Secondly, and most importantly, $\delta\bar{T}_\phi/\delta\bar{T}_\theta$ strongly decreases with decreasing E as does the variability between different imposed patterns (Fig. 5d). At $E = 10^{-6}$ latitudinal variations at the IB are stronger than longitudinal variations by an order of magnitude and do not depend significantly on the pattern or amplitude of the boundary forcing.

Another measure of the thermal heterogeneity induced by the OB anomalies is to compare the maximum longitudinal variation in $\bar{T}$, $\delta\bar{T}_\phi$, for heterogeneous and homogeneous cases. At the OB the ratio $\delta\bar{T}_\phi^{het}/\delta\bar{T}_\phi^{hom} \approx 2-6$ (Fig. 6a), while at the IB $\delta\bar{T}_\phi^{het}/\delta\bar{T}_\phi^{hom} \approx 1-2$ independent of Ra/Ra_c (Fig. 6b). Crucially,

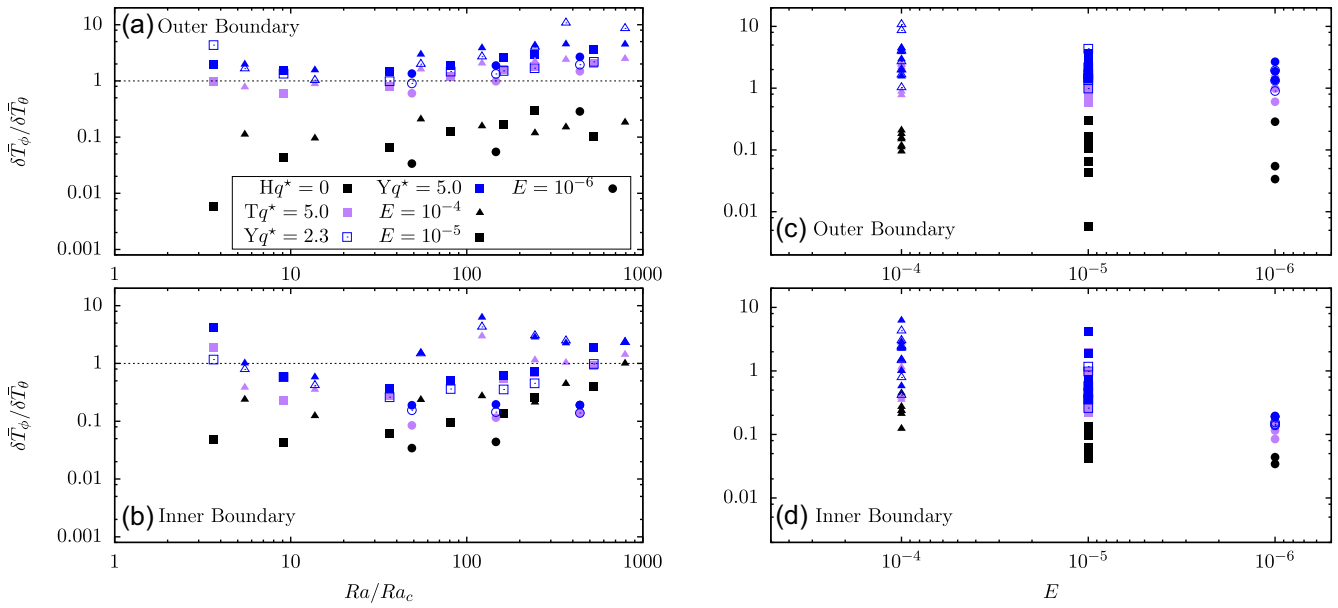

Figure 5. Maximum variation in $\bar{T}$ with longitude, $\delta\bar{T}_\phi$, divided by maximum variation of $\bar{T}$ with latitude, $\delta\bar{T}_\theta$, at the OB (top panel) and IB (bottom panel) as a function of supercriticality Ra/Ra_c (left-hand panel) and E (right-hand panel). Shape distinguishes the value of E; colour distinguishes the pattern of outer boundary heat flow; open and closed symbols show models with $q^\star = 2.3$ and $q^\star = 5.0$, respectively. Tomographic models with $q^\star = 2.3$ have been omitted for clarity; they plot below the T$q^\star = 5.0$ models.

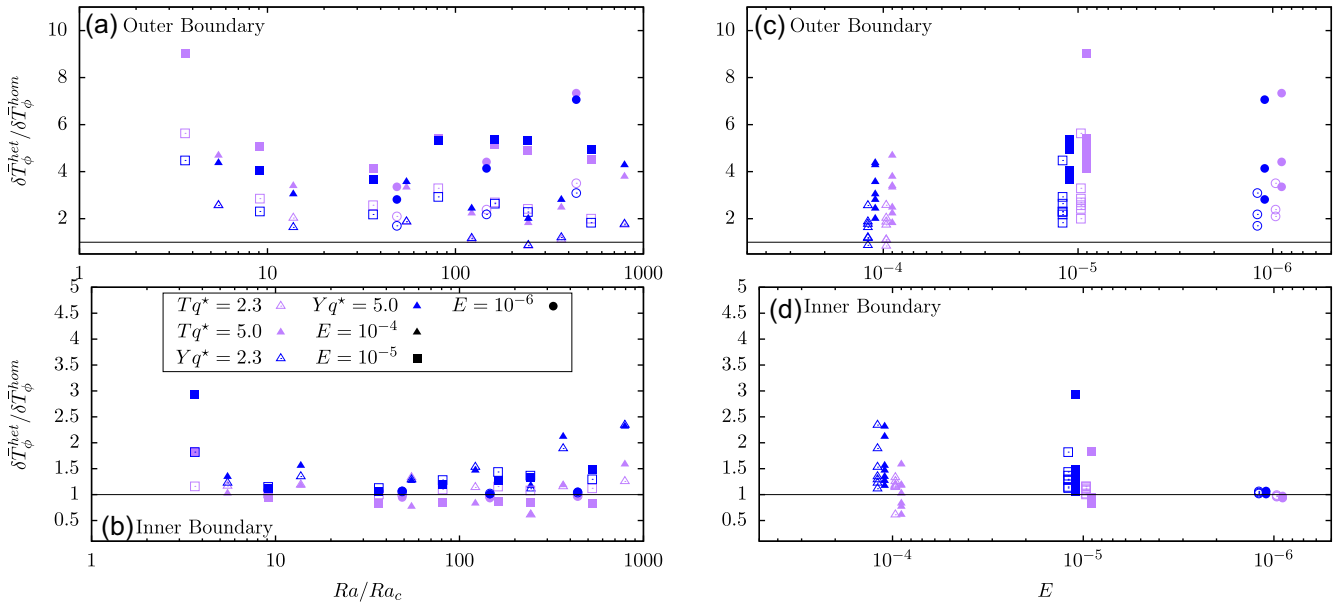

Figure 6. Maximum longitudinal variation in $\bar{T}$, $\delta\bar{T}_\phi$, for heterogeneous cases divided by the corresponding value for the homogeneous case at the same E and Ra/Ra_c at the OB (top panel) and IB (bottom panel) as a function of supercriticality, Ra/Ra_c (left-hand panel) and E (right-hand panel). Shape distinguishes the value of E; colour distinguishes the pattern of outer boundary heat flow; open and closed symbols show models with $q^\star = 2.3$ and $q^\star = 5.0$, respectively. In panels (c) and (d) small offsets in E have been applied for clarity.

longitudinal temperature variations at the IB are almost identical between homogeneous and heterogeneous models at $E = 10^{-6}$ independent of the pattern and amplitude of boundary heterogeneity within the ranges considered (Fig. 6d).

4 DISCUSSION

Our simulations indicate that the impact of OB heat flow anomalies on the time-averaged temperature, $\bar{T}$, is very different at the top of the fluid shell compared to the base of the shell. At the OB, latitudinal and longitudinal variations of $\bar{T}$ in heterogeneous models greatly exceed variations in the corresponding homogeneous model, with the main anomalies located in the equatorial region. At low E ($\leq 10^{-5}$) and high Ra ($\geq 100 Ra/Ra_c$) the longitudinal anomalies exceed the latitudinal anomalies on the OB. In contrast, at the IB, the latitudinal variation in $\bar{T}$ is very similar between homogeneous and heterogeneous cases. Longitudinal variations in $\bar{T}$ for heterogeneous cases are distinguishable from the homogeneous cases at the highest values of E considered, but become indistinguishable as

E decreases and Ra increases. Indeed, in our $E = 10^{-6}$ cases the latitudinal variation of $\bar{T}$ strongly exceeds the longitudinal variations at all values of Ra up to $Ra = 435Ra_c$.

We have noted that homogeneous solutions with $E = 10^{-4}$ display much stronger latitudinal and longitudinal variations than models at lower E and heterogeneous $E = 10^{-4}$ models display maximum IB temperature at the equator rather than a minimum as seen at lower E. These differences are important when interpreting morphological characteristics of the temperature fields in these models since such features evidently do not persist into the lower E regime that is more appropriate to planetary cores.

Before considering the potential consequences of our results for Earth's core we must evaluate limitations in the modelling approach. Our suite of models is one of the largest created to study boundary heat flow variations in spherical shell rotating convection that systematically spans (E, Ra)-space, reaching values near the cutting edge of what is presently possible with direct numerical simulations. On the other hand it is still impossible to access the values of $E \sim 10^{-13} - 10^{-16}$ and $Ra \sim 10^{17}$ estimated for the core (e.g. Mound *et al.* 2019) based on molecular properties of iron at high pressure and temperature (e.g. Davies *et al.* 2015) and so extrapolation from simulations is inevitable.

The value of $q^\star$ is also highly uncertain. Estimates of mantle thermal conductivity coupled with seismic tomography suggest that the CMB heat flow ranges from 0 to 140 mW m^{-2} (Stackhouse *et al.* 2015), which is consistent with predictions from some global mantle circulation models (Nakagawa & Tackley 2007; Olson *et al.* 2015). The mean superadiabatic heat flow at the CMB $q_{\rm ave}$ depends on the difference between the total CMB heat flow, which is estimated to lie between 5 and 17 TW (Lay *et al.* 2009; Nimmo 2015; Jaupart *et al.* 2015), and the adiabatic heat flow, which is 4−16 TW depending on the assumed value of the core thermal conductivity (Davies *et al.* 2015). Estimates of $q_{\rm ave}$, and hence $q^\star$, can therefore take either sign, and as a consequence of its definition $q^\star$ becomes infinite if the top of the core is neutrally stable. An alternative estimate of $q_{\rm ave}$ is obtained by balancing inertial, Coriolis and buoyancy terms in the vorticity equation. The resulting estimates of the flow speed are supported by dynamo simulations (Christensen & Aubert 2006), which translate into a value of $q_{\rm ave} \sim 4$ mW m^{-2} (Jones 2011). Using this estimate together with the values of $q_{\rm max} - q_{\rm min}$ discussed above implies that $q^\star$ could be as large as 35. By comparison, numerical studies have tended to focus on lower values: the regime $q^\star \leq 1$ has been explored in detail (e.g. Zhang & Gubbins 1993; Aubert *et al.* 2007, 2008; Davies *et al.* 2009; Dietrich *et al.* 2016), while some studies have considered values of $q^\star$ up to approximately 2 (Olson & Christensen 2002; Sreenivasan 2009; Sahoo & Sreenivasan 2017). Laboratory experiments have studied strong boundary forcing with $q_{\rm max}/q_{\rm ave} \leq 95$ (Sumita & Olson 2002).

At the OB, Figs 5 and 6 show that $\delta\bar{T}_\phi/\delta\bar{T}_\theta$ and $\delta\bar{T}_\phi^{het}/\delta\bar{T}_\phi^{hom}$ display a weak dependence on Ra and E and increase with $q^\star$ and the lengthscale L of the imposed heat flow pattern. This is consistent with previous studies that have found the effect of boundary anomalies tends to strengthen as $q^\star$ and L increase (Zhang & Gubbins 1993; Davies *et al.* 2009; Calkins *et al.* 2015). Since we expect $q^\star$ to be larger in Earth than in our models, the results suggest that longitudinal temperature variations would exceed latitudinal temperature variations and be clearly distinguishable from temperature anomalies due to homogeneous convection at core conditions.

By contrast, at the IB, Figs 5 and 6 show that $\delta\bar{T}_\phi/\delta\bar{T}_\theta$ and $\delta\bar{T}_\phi^{het}/\delta\bar{T}_\phi^{hom}$ are almost independent of Ra and L at high Ra, increase with $q^\star$ (though to a lesser extent than at the OB) and decrease strongly as E decreases. At low E and high Ra it is clear that latitudinal temperature variations dominate longitudinal variations at the IB and that the longitudinal variations induced by the imposed heat flow are indistinguishable from those that arise due to homogeneous convection. Since the E effect dominates in our simulations we would expect these conclusions to be reinforced upon moving to the lower E regime that characterizes Earth's core.

Sumita & Olson (2002) observed large-scale spiralling jets that reached the IB at somewhat similar conditions to those used here. They conducted rotating convection experiments in a hemispherical shell with $E = 2.4 \times 10^{-6}$, $Ra_T/Ra_c \leq 62$ and $q_{\rm max}/q_{\rm ave} \leq 95$ and applied heterogeneous forcing through localized heat sources on the OB. Here Ra_T is a Rayleigh number based on an imposed temperature difference, rather than the flux-based Rayleigh number used in the present simulations. Sumita & Olson (2002) found that the radial scale of the jets was sensitive to the location and pattern of boundary heating; in particular, they observed that jets do not penetrate to the IB when an isolated boundary heat source is placed at low latitudes or when two heat sources are placed at antipodal locations. This may explain why such jets are not observed in our simulations, which have the strongest heat flow anomalies in the equatorial region and contain regions of anomalously high and anomalously low heat flow.

The strong reduction of persistent IB thermal anomalies with E in our models arises because of the disparity between the characteristic lengthscales of the flow, l, and the boundary forcing, L. It is well known that the influence of thermal boundary forcing on the global dynamics is most significant when $L = l$, in which case the whole flow pattern can become locked to the pattern of boundary heterogeneity (Zhang & Gubbins 1993). When $L \approx l$ quasi-locked solutions can be found at low Ra (e.g. Willis *et al.* 2007; Sreenivasan 2009), but as E (and therefore l) decreases all solutions become time-dependent (Davies *et al.* 2009). The heat that is transported near the boundary by the large-scale thermal wind flow (Sreenivasan 2009) is advected into the deeper interior by flow of much smaller scale and correspondingly shorter diffusion time, thereby reducing the probability that advective flow will retain its morphological identity all the way to the IB.

Another effect that stifles the transfer of the large-scale OB pattern to the IB is the emergence of a zonal flow at high Ra. This flow is aligned with the rotation axis and, in nonmagnetic convection, is strong and retrograde outside the inner core (Christensen 2002; Aubert 2005). The zonal flow shears convective anomalies and sweeps them around the inner core, smearing out any longitudinal variations that would arise in its absence.

It is worth considering effects not included in our simulations that might alter the lengthscale of the deep flow. Our simulations do not include a self-generated magnetic field, which reduces computational costs and allows systematic exploration of the low E, high Ra regime. A body of work now suggests that the appropriate dynamical balance at core conditions is between the pressure gradient and Coriolis effect at zeroth order (geostrophy) and between magnetic, Archimedian (buoyancy) and Coriolis terms at first order (MAC balance) (Davidson 2013; Aubert *et al.* 2017; Aurnou & King 2017; Schaeffer *et al.* 2017; Calkins 2018). In this regime the magnetic field is expected to partly offset the rotational con-

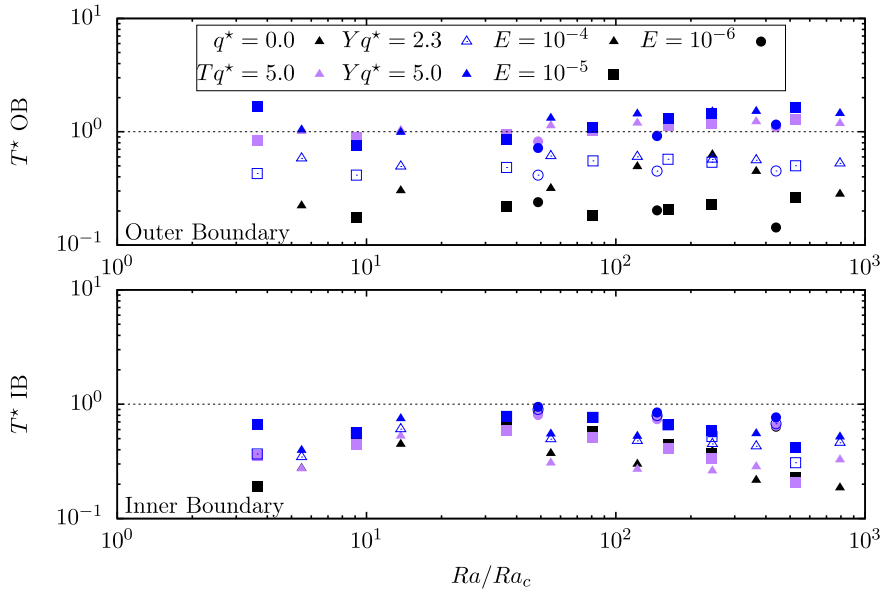

Figure 7. $T^\star$ at the OB (top panel) and IB (bottom) as a function of supercriticality, Ra/Ra_c. Shape distinguishes the value of E; colour distinguishes the pattern of outer boundary heat flow; open and closed symbols show models with $q^\star = 2.3$ and $q^\star = 5.0$, respectively. Tomographic models with $q^\star = 2.3$ have been omitted for clarity; they plot below the $Tq^\star = 5.0$ models.

Table 1. Empirical fits $T^\star = (Ra/Ra_c)^a 10^b$ to the data in Fig. 7 for different E and imposed heat flow boundary conditions. The top section shows results for the OB; the bottom section shows results for the inner boundary. The boundary conditions (BC) are labelled homogeneous (H), tomographic (T) and hemispheric (Y) followed by the imposed amplitude $q^\star$. The final two columns give values of $T^\star$ extrapolated using the fitting parameters a and b to $Ra/Ra_c = 10^3$ and $Ra/Ra_c = 10^8$, respectively.

E	BC	a	b	$T^\star$ ($Ra/Ra_c = 10^3$)	$T^\star$ ($Ra/Ra_c = 10^8$)
10^{-5}	H	0.164	−1.017	0.299	1.99
10^{-6}	H	−0.234	−0.211	0.121	0.01
10^{-5}	T$q^\star = 2.3$	0.015	−0.292	0.567	0.68
10^{-5}	Y$q^\star = 2.3$	0.055	−0.402	0.581	1.10
10^{-6}	T$q^\star = 2.3$	−0.002	−0.301	0.492	0.48
10^{-6}	Y$q^\star = 2.3$	0.039	−0.443	0.472	0.74
10^{-5}	T$q^\star = 5.0$	0.086	−0.138	1.319	3.57
10^{-5}	Y$q^\star = 5.0$	0.057	−0.020	1.416	2.74
10^{-6}	T$q^\star = 5.0$	0.132	−0.312	1.216	5.59
10^{-6}	Y$q^\star = 5.0$	0.216	−0.507	1.384	16.7
10^{-5}	H	0.017	−0.441	0.409	0.50
10^{-6}	H	−0.122	0.134	0.584	0.14
10^{-5}	T$q^\star = 2.3$	0.021	−0.412	0.450	0.58
10^{-5}	Y$q^\star = 2.3$	−0.006	−0.257	0.528	0.49
10^{-6}	T$q^\star = 2.3$	−0.097	0.074	0.604	0.20
10^{-6}	Y$q^\star = 2.3$	−0.096	0.139	0.707	0.23
10^{-5}	T$q^\star = 5.0$	−0.089	−0.252	0.301	0.11
10^{-5}	Y$q^\star = 5.0$	−0.047	−0.120	0.544	0.31
10^{-6}	T$q^\star = 5.0$	−0.133	0.145	0.557	0.12
10^{-6}	Y$q^\star = 5.0$	−0.130	0.176	0.611	0.14

straint, supporting flows of larger lengthscale than would arise in its absence (e.g. Chandrasekhar 1961; Sakuraba & Roberts 2009; Dormy 2016; Yadav *et al.* 2016), which might help to transfer CMB heat flow anomalies to the deeper core. On the other hand, strong magnetic fields tend to reduce the axial alignment of convective structures (Dormy 2016; Yadav *et al.* 2016), which might hinder the propagation of OB effects to depth. Future dynamo simulations with heterogeneous boundary conditions are needed to quantify the relative importance of these effects.

Magnetic fields also significantly alter the zonal flow. Aubert (2005) found prograde zonal flows in his simulations, which would still act to smear out the effect of OB anomalies as in our models. In non-magnetic convection the zonal flow is dominantly columnar and draws its power from the non-axisymmetric flow via the Reynolds stress; however, in dynamo simulations the magnetic field can break the axial alignment, in which case the zonal flow is powered by the thermal wind (Aubert 2005). Different scaling behaviour for the zonal flow speed is predicted in the two cases. In the simulations the zonal flow is weakened by the magnetic field (Aubert 2005; Schaeffer *et al.* 2017), and the scaling behaviour predicts that the dynamo-generated zonal flow would be slower at core conditions than the non-magnetic zonal flow [see eqs (3.1) and (3.2) of Aubert

2005]. However, the scaling law of Aubert (2005) predicts a zonal flow velocity of $\sim 10^{-4}$ m s^{-1} in the core and so the time taken for one revolution of the zonal flow around the inner core is comparable to the time for fluid parcels to descend from the CMB to the ICB. Therefore it is possible that the smearing effect could be important in the core.

Figs 5 and 6 do not allow a simple interpretation of the amplitude of lateral thermal variations because $\delta\bar{T}_\theta$ and $\delta\bar{T}_\phi^{hom}$ are poorly known for the core. To estimate the amplitude we derive empirical scalings based on $T^\star$ at the OB and IB (Fig. 7). At the OB $T^\star$ increases with increasing $q^\star$ and is approximately constant with E and Ra. At the IB $T^\star$ is much less sensitive to the OB heat flow pattern and $q^\star$ and decreases with Ra/Ra_c at high Ra. These observations suggest fitting $T^\star$ to a function of the form $(Ra/Ra_c)^a 10^b$. The dependence of $T^\star$ on the heat flow pattern is not simple, while the three values of E in our suite of simulations do not allow a robust estimate of the E-dependence of $T^\star$. Therefore we empirically fit $T^\star$ for each $q^\star$, E and heat flow pattern. Results are given in Table 1, which also provides values of $T^\star$ extrapolated to $Ra/Ra_c = 10^3$ and 10^8, which span the range of plausible estimates provided by Gubbins (2001). Note that the extrapolation to $Ra/Ra_c = 10^8$ at higher E should be interpreted with caution since such high values of Ra/Ra_c may not lie in the rapidly rotating regime thought appropriate for core dynamics.

As expected, the results in Table 1 show weak Ra dependence at both the OB and IB, while the E-dependence is weaker at the OB than at the IB. The extrapolated values of $T^\star$ can exceed 10 at the OB for the most extreme cases and are always <1 at the IB. To estimate $\max(\bar{T}) - \min(\bar{T})$ for the Earth we assume $\Delta T = 10^{-3}$ K, the lower end of estimates given in Section 1. In this case the lateral thermal anomalies in the core are estimated to be a few mK at the core–mantle boundary and around one tenth of a mK at the inner core boundary. However, at the OB, changing $q^\star$ from 2.3 to 5.0 increases the predicted value of $T^\star$ by an order of magnitude or more. The trend with increasing $q^\star$ is difficult to determine from our dataset. If the change in $T^\star$ scales like $(q^\star)^2$ then extrapolating to $q^\star = 35$ would suggest $T^\star \sim 10^2 - 10^3$ and lateral temperature anomalies of $\sim 0.01 - 0.1$ K; if $T^\star$ scales like $q^\star$ then $T^\star \sim 10^3 - 10^4$ at $q^\star = 35$. These values are comparable with estimates from geodynamo simulations for the temperature anomalies arising from penetration of boundary heat flow anomalies into a stable layer below the OB (Christensen 2018). At the IB, at sufficiently low E, the amplitude of lateral variations is insensitive to the pattern or amplitude of OB heat flow. Therefore temperature anomalies at the ICB are expected to be comparable to those arising in homogeneous convection, nominally $O(10^{-4})$ K.

5 CONCLUSIONS

We have studied non-magnetic convection in a rotating spherical shell with lateral heat flow variations imposed at the OB. Our study covers the parameter range $10^{-4} \leq E \leq 10^{-6}$, $1 \leq Ra/Ra_c \leq 800$ and considers Y_1^1 and tomographic heat flow patterns with amplitudes measured by the parameter $q^\star = 2.3$, 5 as well as the homogeneous case with $q^\star = 0$. We have focused on the time-averaged temperature anomalies produced at the IB and OB of the fluid shell. We find that:

(i) At the OB, latitudinal and longitudinal temperature variations induced by the boundary forcing greatly exceed variations produced by homogeneous convection and are most prominent in the equatorial region. Longitudinal variations exceed latitudinal anomalies; based on empirical scaling estimates they are weakly dependent on E and Ra and may reach $O(1)$ K if the forcing is strong. Such strong temperature variations may be seismically observable and searching for lateral variations in seismic velocity near the top of the core may provide new constraints on the amplitude of temperature variations induced by CMB heterogeneity.

(ii) At the IB, boundary-induced temperature variations become practically indistinguishable from temperature anomalies due to homogeneous convection as E decreases. In our most extreme models latitudinal variations exceed longitudinal variations. Induced anomalies decrease strongly with E and are weakly dependent on Ra and $q^\star$. Extrapolated to core conditions our results suggest that heat flow variations on the CMB are unlikely to explain the large-scale variations observed by seismology at the top of the inner core.

ACKNOWLEDGEMENTS

CD acknowledges a Natural Environment Research Council personal fellowship, reference NE/L011328/1. This work used the ARCHER UK National Supercomputing Service (http://www.archer.ac.uk) and ARC2, part of the High Performance Computing facilities at the University of Leeds, UK. We are grateful for the constructive comments provided by two reviewers.

REFERENCES

Aubert, J., 2005. Steady zonal flows in spherical shell dynamos, *J. Fluid Mech.,* **542,** 53–67.

Aubert, J., Amit, H. & Hulot, G., 2007. Detecting thermal boundary control in surface flows from numerical dynamos, *Phys. Earth planet. Int.,* **160,** 143–156.

Aubert, J., Amit, H., Hulot, G. & Olson, P., 2008. Thermochemical flows couple the Earth's inner core growth to mantle heterogeneity, *Nature,* **454,** 758–761.

Aubert, J., Gastine, T. & Fournier, A., 2017. Spherical convective dynamos in the rapidly rotating asymptotic regime, *J. Fluid Mech.,* **813,** 558–593.

Aurnou, J. & King, E., 2017. The cross-over to magnetostrophic convection in planetary dynamo systems, *Phil. Trans. R. Soc. Lond., A,* **473**(2199), doi:10.1098/rspa.2016.0731.

Bloxham, J., 2000. The effect of thermal core-mantle interactions on the palaeomagnetic secular variation, *Phil. Trans. R. Soc. Lond., A,* **358,** 1171–1179.

Bloxham, J. & Gubbins, D., 1987. Thermal core-mantle interactions, *Nature,* **325,** 511–513.

Bloxham, J. & Jackson, A., 1990. Lateral temperature variations at the core-mantle boundary deduced from the magnetic field, *Geophys. Res. Lett.,* **17,** 1997–2000.

Brodholt, J. & Badro, J., 2017. Composition of the low seismic velocity E' layer at the top of Earth's core, *Geophys. Res. Lett.,* **44**(16), 8303–8310.

Buffett, B., 2007. Core-mantle interactions, in *Treatise on Geophysics,* Vol. **8,** Core Dynamics, pp. 213–224, ed. Schubert, G., Elsevier.

Calkins, M., 2018. Quasi-geostrophic dynamo theory, *Phys. Earth planet. Int.,* **276,** 182–189.

Calkins, M., Hale, K., Julien, K., Nieves, D., Driggs, D. & Marti, P., 2015. The asymptotic equivalence of fixed heat flux and fixed temperature thermal boundary conditions for rapidly rotating convection, *J. Fluid Mech.,* **784,** R2.

Chandrasekhar, S., 1961. *Hydrodynamic and Hydromagnetic Stability International Series of Monographs on Physics*. Dover.

Christensen, U., 2002. Zonal flow driven by strongly supercritical convection in rotating spherical shells, *J. Fluid Mech.,* **470,** 115–133.

Christensen, U., 2018. Geodynamo models with a stable layer and heterogeneous heat flow at the top of the core, *Geophys. J. Int.,* **215**(2), 1338–1351.

Christensen, U. & Aubert, J., 2006. Scaling properties of convection-driven dynamos in rotating spherical shells and application to planetary magnetic fields, *Geophys. J. Int.,* **166,** 97–114.

Christensen, U. & Olson, P., 2003. Secular variation in numerical geodynamo models with lateral variations of boundary heat flow, *Phys. Earth planet. Int.,* **138,** 39–54.

Davidson, P., 2013. Scaling laws for planetary dynamos, *Geophys. J. Int.,* **195**(1), 67–74.

Davies, C., Gubbins, D. & Jimack, P., 2009. Convection in a rapidly rotating spherical shell with an imposed laterally varying thermal boundary condition, *J. Fluid Mech.,* **641,** 335–358.

Davies, C., Gubbins, D. & Jimack, P., 2011. Scalability of pseudospectral methods for geodynamo simulations, *Concurr. Comput.: Pract. Exper,* **23,** 38–56.

Davies, C., Gubbins, D., Willis, A. & Jimack, P., 2008. Time-averaged paleomagnetic field and secular variation: predictions from dynamo solutions based on lower mantle seismic tomography, *Phys. Earth planet. Int.,* **169,** 194–203.

Davies, C., Pozzo, M., Gubbins, D. & Alfè, D., 2015. Constraints from material properties on the dynamics and evolution of Earth's core, *Nat. Geosci.,* **8,** 678–687.

Dietrich, W., Hori, K. & Wicht, J., 2016. Core flows and heat transfer induced by inhomogeneous cooling with sub-and supercritical convection, *Phys. Earth planet. Int.,* **251,** 36–51.

Dormy, E., 2016. Strong-field spherical dynamos, *J. Fluid Mech.,* **789,** 500–513.

Garnero, E. & McNamara, A., 2008. Structure and dynamics of Earth's lower mantle, *Science,* **320,** 626–628.

Garnero, E., McNamara, A. & Shim, S.-H., 2016. Continent-sized anomalous zones with low seismic velocity at the base of Earth's mantle, *Nat. Geosci.,* **9,** 481–489.

Gastine, T., Wicht, J. & Aubert, J., 2016. Scaling regimes in spherical shell rotating convection, *J. Fluid Mech.,* **808,** 690–732.

Gillet, N. & Jones, C., 2006. The quasi-geostrophic model for rapidly rotating spherical convection outside the tangent cylinder, *J. Fluid Mech.,* **554,** 343–369.

Grand, S.P., van der Hilst, R. & Widiyantoro, S., 1997. Global seismic tomography: a snapshot of convection in the Earth, *GSA Today,* **7,** 1–7.

Gubbins, D., 2001. The Rayleigh number for convection in the Earth's core, *Phys. Earth planet. Int.,* **128,** 3–12.

Gubbins, D., 2003. Thermal core-mantle interactions: theory and observations, in *Earth's core: Dynamics, Structure, Rotation,* Geodynamics Series 31, pp. 162–179, eds Dehant, V., Creager, K., Karato, S. & Zatman, S., American Geophysical Union.

Gubbins, D., Alfè, D., Masters, G., Price, G. & Gillan, M., 2004. Gross thermodynamics of two-component core convection, *Geophys. J. Int.,* **157,** 1407–1414.

Gubbins, D. & Davies, C., 2013. The stratified layer at the core-mantle boundary caused by barodiffusion of Oxygen, Sulphur and Silicon, *Phys. Earth planet. Int.,* **215,** 21–28.

Gubbins, D., Masters, G. & Nimmo, F., 2008. A thermochemical boundary layer at the base of Earth's outer core and independent estimate of core heat flux, *Geophys. J. Int.,* **174,** 1007–1018.

Gubbins, D., Sreenivasan, B., Mound, J. & Rost, S., 2011. Melting of the Earth's inner core, *Nature,* **473,** 361–364.

Gubbins, D., Willis, A. & Sreenivasan, B., 2007. Correlation of Earth's magnetic field with lower mantle thermal and seismic structure, *Phys. Earth planet. Int.,* **162,** 256–260.

Helffrich, G. & Kaneshima, S., 2010. Outer-core compositional stratification from observed core wave speed profiles, *Nature,* **468,** 807–809.

Hernlund, J. & McNamara, A., 2015. The core-mantle boundary region, in *Treatise on Geophysics,* **Vol. 7,** pp. 461–519, ed. Schubert, G., Elsevier.

Jaupart, C., Labrosse, S. & Mareschal, J.-C., 2015. Temperatures, heat and energy in the mantle of the Earth, in *Treatise on Geophysics,* **Vol. 7,** pp. 223–270, ed. Schubert, G., Elsevier.

Jones, C., 2000. Convection-driven geodynamo models, *Phil. Trans. R. Soc. Lond., A,* **358,** 873–897.

Jones, C., 2011. Planetary magnetic fields and fluid dynamos, *Ann. Rev. Fluid Mech.,* **43,** 583–614.

Jones, C., 2015. Thermal and compositional convection in the outer core, in *Treatise on Geophysics,* Vol. **8,** Chapter 5, pp. 116–159, ed. Schubert, G., Elsevier.

Julien, K., Knobloch, E., Rubio, A. & Vasil, G., 2012a. Heat transport in low-Rossby-number Rayleigh-Bénard convection, *Phys. Rev. Lett.,* **109**(25), 254503.

Julien, K., Rubio, A., Grooms, I. & Knobloch, E., 2012b. Statistical and physical balances in low Rossby number Rayleigh–Bénard convection, *Geophys. Astrophys. Fluid Dyn.,* **106**(4-5), 392–428.

Lay, T., Hernlund, J. & Buffett, B., 2009. Core-mantle boundary heat flow, *Nat. Geosci.,* **1,** 25–32.

Lister, J. & Buffett, B., 1995. The strength and efficiency of thermal and compositional convection in the geodynamo, *Phys. Earth planet. Int.,* **91,** 17–30.

Masters, G., Johnson, S., Laske, G. & Bolton, H., 1996. A shear-velocity model of the mantle, *Phil. Trans. R. Soc. Lond., A,* **354,** 1385–1411.

Matsui, H. *et al.*, 2016. Performance benchmarks for a next generation numerical dynamo model, *Geochem. Geophys. Geosys.,* **17**(5), 1586–1607.

Monnereau, M., Calvet, M., Margerin, L. & Souriau, A., 2010. Lopsided growth of Earth's inner core, *Science,* **328,** 1014–1017.

Mound, J. & Davies, C., 2017. Heat transfer in rapidly rotating convection with heterogeneous thermal boundary conditions, *J. Fluid Mech.,* **828,** 601–629.

Mound, J., Davies, C., Aurnou, J. & Rost, S., 2019. Regional stratification at the top of Earth's core due to core–mantle boundary heat flux variations, In Press, doi:10.1038/s41561-019-0381-z.

Mound, J., Davies, C. & Silva, L., 2015. Inner core translation and the hemispheric balance of the geomagnetic field, *Earth planet. Sci. Lett.,* **424,** 148–157.

Nakagawa, T. & Tackley, P., 2007. Lateral variations in CMB heat flux and deep mantle seismic velocity caused by a thermal-chemical-phase boundary layer in 3D spherical convection, *Earth planet. Sci. Lett.,* **271,** 348–358.

Nimmo, F., 2015. Energetics of the core, in *Treatise on Geophysics,* **Vol. 8,** 2nd edn, pp. 27–55, ed. Schubert, G., Elsevier.

Niu, F. & Wen, L., 2001. Hemispherical variations in seismic velocity at the top of the Earth's inner core, *Nature,* **410,** 1081–1084.

Olson, P., 2003. Thermal interaction of the core and mantle, in *The 7th Symposium on Earth's Core and Lower Mantle, Contributions from the SEDI 2000,* pp. 1–38.

Olson, P. & Christensen, U., 2002. The time-averaged magnetic field in numerical dynamos with non-uniform boundary heat flow, *Geophys. J. Int.,* **151,** 809–823.

Olson, P., Deguen, R., Rudolph, M. & Zhong, S., 2015. Core evolution driven by mantle global circulation, *Phys. Earth planet. Int.,* **243,** 44–55.

Olson, P., Landeau, M. & Reynolds, E., 2017. Dynamo tests for stratification below the core-mantle boundary, *Phys. Earth planet. Int.,* **271,** 1–18.

Sahoo, S. & Sreenivasan, B., 2017. On the effect of laterally varying boundary heat flux on rapidly rotating spherical shell convection, *Phys. Fluids,* **29**(8), 086602.

Sakuraba, A. & Roberts, P., 2009. Generation of a strong magnetic field using uniform heat flux at the surface of the core, *Nat. Geosci.,* **2,** 802–805.

Schaeffer, N., Jault, D., Nataf, H.-C. & Fournier, A., 2017. Turbulent geodynamo simulations: a leap towards Earth's core, *Geophys. J. Int.,* **211**(1), 1–29.

Shishkina, O., Grossmann, S. & Lohse, D., 2016. Heat and momentum transport scalings in horizontal convection, *Geophys. Res. Lett.,* **43**(3), 1219–1225.

Souriau, A. & Calvet, M., 2015. Deep Earth structure – the Earth's cores, in *Treatise on Geophysics,* **Vol. 1,** Chapter 23, pp. 725–757, eds Schubert, G., Romanowicz, B. & Dziewonski, A., Elsevier.

Sreenivasan, B., 2009. On dynamo action produced by boundary thermal coupling, *Phys. Earth planet. Int.,* **177,** 130–138.

Sreenivasan, B. & Gubbins, D., 2011. On mantle-induced heat flow variations at the inner core boundary, *Phys. Earth planet. Int.,* **187**(3-4), 336–341.

Stackhouse, S., Stixrude, L. & Karki, B., 2015. First principles calculations of lattice thermal conductivity of the lower mantle, *Earth planet. Sci. Lett.,* **427,** 11–17.

Stevenson, D., 1987. Limits on lateral density and velocity variations in the Earth's outer core, *Geophys. J. Int.,* **88,** 311–319.

Sumita, I. & Olson, P., 2002. Rotating thermal convection experiments in a hemispherical shell with heterogeneous boundary heat flux: implications for the Earth's core, *J. geophys. Res.,* **107**(B8), ETG 5–1-ETG 5-18.

Sun, Z.-P., Schubert, G. & Glatzmaier, G., 1994. Numerical simulations of thermal convection in a rapidly rotating spherical shell cooled inhomogeneously from above, *Geophys. Astrophys. Fluid Dyn.,* **75,** 199–226.

Waszek, L., Irving, J. & Deuss, A., 2011. Reconciling the hemispherical structure of Earth's inner core with its super-rotation, *Nat. Geosci.,* **4,** 264–267.

Willis, A., Sreenivasan, B. & Gubbins, D., 2007. Thermal core-mantle interaction: exploring regimes for 'locked' dynamo action, *Phys. Earth planet. Int.,* **165,** 83–92.

Wong, J., Davies, C. & Jones, C., 2018. A Boussinesq slurry model of the F-layer at the base of Earth's outer core, *Geophys. J. Int.,* **214,** 2236–2249.

Yadav, R., Gastine, T., Christensen, U., Duarte, L. & Reiners, A., 2015. Effect of shear and magnetic field on the heat-transfer efficiency of convection in rotating spherical shells, *Geophys. J. Int.,* **204**(2), 1120–1133.

Yadav, R., Gastine, T., Christensen, U., Wolk, S. & Poppenhaeger, K., 2016. Approaching a realistic force balance in geodynamo simulations, *Proc. Natl. Acad. Sci.,* **113**(43), 12065–12070.

Zhang, K. & Gubbins, D., 1992. On convection in the Earth's core driven by lateral temperature variations in the lower mantle, *Geophys. J. Int.,* **108,** 247–255.

Zhang, K. & Gubbins, D., 1993. Convection in a rotating spherical fluid shell with an inhomogeneous temperature boundary condition at infinite Prandtl number, *J. Fluid Mech.,* **250,** 209–232.

Zhang, K. & Gubbins, D., 1996. Convection in a rotating spherical fluid shell with an inhomogeneous temperature boundary condition at finite Prandtl number, *Phys. Fluids,* **8,** 1141–1148.

Zhong, S., Yuen, D. & Moresi, L., 2007. Numerical methods for mantle convection, in *Treatise on Geophysics,* **Vol. 7,** Chapter 5, pp. 227–252, ed. Schubert, G., Elsevier.